# Comparison of Passive Microwave Ice Concentration Algorithm Retrievals With AVHRR Imagery in Arctic Peripheral Seas

Walter N. Meier

***Abstract*—An accurate representation of sea ice concentration is valuable to operational ice analyses, process studies, model inputs, and detection of long-term climate change. Passive microwave imagery, such as from the Special Sensor Microwave/Imager (SSM/I), are particularly valuable for monitoring of sea ice conditions because of their daily, basin-scale coverage under all sky conditions. SSM/I-derived sea ice concentration estimates using four common algorithms [Bootstrap (BT), Cal/Val (CV), NASA Team (NT), and NASA Team 2 (N2)] are compared with concentrations computed from Advanced Very High Resolution Radiometer (AVHRR) visible and infrared imagery. Comparisons are made over approximately an eight-month period in three regions of the Arctic and focus on areas near the ice edge where differences between the algorithms are likely to be most apparent. The results indicate that CV and N2 have the smallest mean error relative to AVHRR. CV tends to overestimate concentration, while the other three algorithms underestimate concentration. NT has the largest underestimation of nearly 10% on average and much higher in some instances. In most cases, mean errors of the SSM/I algorithm were significantly different from each other at the 95% significance level. The BT algorithm has the lowest error standard deviation, but none of the considered algorithms was found to have statistically significantly different error standard deviations in most cases. This indicates that spatial resolution is likely a limiting factor of SSM/I in regions near the ice edge in that none of the algorithms satisfactorily resolve mixed pixels. Statistical breakdowns by season, region, ice conditions, and AVHRR scene generally agree with the overall results. Representative case studies are presented to illustrate the statistical results.**

***Index Terms*—Arctic regions, algorithms, image sensors, microwave radiometry, sea ice.**

## I. Introduction

SEA ICE plays an important role in global climate and in human activities in the polar regions. Passive microwave imagery has been a valuable source of information on sea ice cover in the polar oceans for over 25 years. Passive microwave sensors are particularly useful because, unlike visible and infrared sensors, they can provide complete daily coverage of the polar regions under all sky conditions.

Since 1978, the Scanning Multichannel Microwave Radiometer (SMMR) and the Special Sensor Microwave/Imager (SSM/I) have provided daily estimates of sea ice extent and sea ice concentration. The over 25-year record of ice conditions is beginning to allow the detection of possible climate change signals in the ice. Analysis has indicated a significant decreasing trend in summer Arctic sea ice extent [1]–[4] and a slight increase in Antarctic extent [4]–[6]. Passive microwave-derived concentrations have also been employed to investigate anomalous ice conditions (e.g., [7] and [8]) in specific years or regions.

Passive microwave sea ice products also provide valuable information for operational ice analyses. These analyses, such as those produced by the U.S. National Ice Center, generally rely on imagery from high resolution visible, infrared, or synthetic aperture radar sensors. However, when such imagery is unavailable (due to clouds and/or lack of satellite coverage), the spatial coverage and all-sky capability of passive microwave sensors provide a crucial complement for producing complete hemispheric analyses.

Sea ice coverage also plays an important role in heat and moisture transfer in the ocean–ice–atmosphere system. Changes in ice concentration can greatly affect latent, sensible, and longwave radiative heat transfer during the winter; changes during the summer also affect the amount of absorbed solar radiation.

Over the years, several previous studies have evaluated ice concentrations from passive microwave imagery in both the Arctic and Antarctic via comparisons with visible and infrared imagery (e.g., [6], [9]–[14]). These evaluations have primarily consisted of case-study evaluations consisting of a few scenes over a short time period in one or two locations and have focused on the evaluation of a single algorithm or an intercomparison of two algorithms. A recent study compared passive microwave ice concentrations with openings from SAR-derived ice motion [15], but it focused on perennial ice-covered areas in the central Arctic Ocean.

Two recent studies have compared passive microwave concentrations with operational ice charts produced from manual interpretation of visible, infrared and synthetic aperture radar imagery as well as ancillary sources such as ship reports and aircraft reconnaissance [16], [17]. These studies benefit from the ability to conduct longer term comparisons over a wider area. However, the ice charts are conglomerations of imagery sources, the quantity and quality of which varies. Also, in the case of the U.S. National Ice Center (NIC) analyses [17], SSM/I imagery has been employed to produce the analyses where other imagery was unavailable, so the two products are not necessarily independent.

The work presented here extends previous SSM/I algorithm evaluations by: 1) using four well-known algorithms; 2) encompassing roughly eight months of collected imagery; 3) cov-

Manuscript received February 13, 2004; revised September 20, 2004.

The author is with the National Snow and Ice Data Center, University of Colorado, Boulder, CO 80309 USA (e-mail: walt@nsidc.org).

Digital Object Identifier 10.1109/TGRS.2005.846151

ering three regions, each with distinct ice conditions; and 4) primarily limiting the comparisons to areas near the ice edge (within $\sim$ 500 km), where differences between the passive microwave algorithms are generally most apparent [10].

## II. Passive Microwave Signature of Sea Ice

The electromagnetic properties of sea ice are a function of the physical properties of the ice (e.g., crystal structure, salinity, temperature, snow cover). The emissive character also changes depending on the microwave frequency, but in general, the passive microwave sea ice signal at a given frequency and polarization is distinct from that of open water. The unfrozen water surface is highly reflective in the microwave regime and thus is typically radiometrically cold; additionally, microwave emission from water is strongly polarized [18]. When salt water freezes, the emissive character of the surface changes substantially. First-year sea ice (ice that has formed since the last melt season) is strongly emissive, but with the emission weakly polarized. As ice ages, saline brine trapped within the ice drains, particularly during summer melt, and the emissive character of the ice changes. Thus multiyear ice (ice that has survived at least one melt season) has a more complex radiative signature, generally with an emissivity and polarity between first-year ice and water. Snow cover on top of the sea ice can substantially modify the microwave signal by scattering of the emission from the underlying ice as well as through direct emission from the snow, particularly under melt conditions [18].

The atmosphere also emits microwave energy and at some frequencies this emission can substantially modify the signal received by the satellite under certain conditions [19], [20]. At frequencies used for sea ice retrievals, the atmospheric emission is primarily due to water vapor and liquid water. Thus high humidity, clouds, and especially rainfall, can result in emission that yields an opaque atmosphere at SSM/I frequencies. Fortunately, the polar regions are generally dry and, at least during the winter, water in the atmosphere is often in a frozen state (though supercooled liquid, which has a more substantial effect on the signal from the surface emission, is also common). Under melt conditions, significant emission will come from the liquid water (meltponds, wet snow) on the surface instead of the underlying ice. These effects can limit the accuracy of satellite-retrieved passive microwave ice products. While the summer melt effects can be substantial, on a basin-scale the surface and atmospheric effects are generally small during winter, allowing for an accurate representation of the overall ice conditions during the cold seasons In summer, such effects can substantially degrade sea ice concentration estimates, though estimates of sea ice extent are less affected.

## III. Special Sensor Microwave/Imager

The first SSM/I was launched aboard the Defense Meteorological Satellite Program (DMSP) F-8 mission in 1987. A series of SSM/I sensors on subsequent DMSP satellites has provided a continuous data stream since then. SSM/I has seven channels at four frequencies. The 19-, 37-, and 85-GHz frequencies are dual polarized (horizontal and vertical); the 22-GHz frequency has only a single vertically polarized channel.

TABLE I
Summary of SSM/I Sea Ice Concentration Algorithm Characteristics

| *Algorithm* | *Primary Channels* | *Secondary Channels* | *Tiepoints* |
|---|---|---|---|
| Bootstrap (BT) | 37V, 37H (multiyear ice) | 19V, 37V (first-year ice) | Winter, multiple summer |
| Cal/Val (CV) | 19V, 37V (within pack) | 37V, 37H (near edge) | Winter, summer |
| NASA Team (NT) | 19V, 19H, 37V | same | Winter, summer |
| NASA Team 2 (N2) | 19V, 19H, 37V, 85V, 85H | same | Winter, summer |

A polar orbit and 1400-km swath width provides near-complete coverage at least once per day in the polar regions. The footprint (instantaneous field of view) of the sensor varies with frequency, ranging from the $69 \times 43$ km footprint of the 19-GHz channels to the $15 \times 13$ km footprint of the 85-GHz channels. Because of the large sensor footprint, small-scale details of the ice cover, such as individual floes, leads, and small polynyas cannot be identified using SSM/I; the large footprint also limits the precision of the ice edge estimate.

For this study, SSM/I swath data was acquired from the National Oceanic and Atmospheric Administration (NOAA) in near-real time at the NIC; this is the operational data stream used for the NIC analyses. Daily (24-h) brightness temperature drop-in-the-bucket composites were created on a polar stereographic projection, with a gridded resolution (pixel size) of 12.5-km for the 85-GHz channels and 25-km for all other channels. The projection, gridding, and compositing method is essentially the same used by the National Snow and Ice Data Center (NSIDC) to create their standard polar stereographic products [21].

## IV. Algorithm Descriptions

The four algorithms investigated in this study are the Comiso Bootstrap (BT), the Cal/Val (CV), the NASA Team (NT), and the Enhanced NASA Team, commonly called the NASA Team 2 (N2). The algorithms rely on tiepoints: empirically derived brightness temperature values for pixels of pure surface types (i.e., 100% ice, 100% water); pixels with pure surface types are selected from comparisons with *in situ* data or other satellite imagery (e.g., visible/infrared or radar). The tiepoints essentially establish baselines for sea ice and water and sea ice concentration is estimated by the algorithms, assuming a mixture of ice and water within each pixel. Due to the uncertainties in the microwave signature discussed above, these hemispheric tiepoints may not be representative of specific conditions [22]. Errors will also result if there is variation in the distinct surface types. For example, in the marginal ice zone (MIZ), new, thin ice is common. Thin ice has a distinct microwave signature compared to the thicker ice used to derive the tiepoints, and this can result in an underestimation of total ice concentration. Table I outlines the SSM/I frequencies and other information for each algorithm and a short summary of each algorithm is

provided below; details on each algorithm can be found in the accompanying references.

### A. Bootstrap

The Comiso Bootstrap algorithm [23], hereafter referred to simply as the Bootstrap algorithm, uses linear combinations of the horizontal and vertical polarizations of the 37-GHz frequency (called the polarization mode) over most of the Arctic. In regions where first-year ice dominates, the vertical polarization of the 19- and 37-GHz frequencies (called the frequency mode) are used. The Bootstrap uses seasonally based tiepoints to improve performance during summer melt conditions. Comiso *et al.* [10] discuss the Bootstrap algorithm and differences between it and the NASA Team algorithm in much further detail. Along with the NASA Team algorithm, the Bootstrap is one of the most commonly used algorithms and is archived at the NSIDC. It is also now the operational algorithm used by the NIC for the Antarctic and is an algorithm included in the Earth Observing System-Aqua/Advanced Microwave Scanning Radiometer-EOS (AMSR-E) products.

### B. Cal/Val

The Cal/Val algorithm [24] is a modified version of the AES-York algorithm [25]. It was developed for the initial calibration/validation of the SSM/I sensor. Within the ice pack, the algorithm uses a linear combination of the vertically polarized 19- and 37-GHz channels. Near the ice edge, the vertically and horizontally polarized 37-GHz channels are employed. Because the footprint (instantaneous field of view) of the 37-GHz channel ($37 \times 28$ km) is smaller than the 19-GHz channel ($69 \times 43$ km), Cal/Val can potentially yield a more precise ice edge [9]. However, the horizontally polarized 37-GHz channel is more susceptible to atmospheric influences than the vertically polarized 19-GHz channel it replaces [20].

The Cal/Val algorithm is designed to be particularly sensitive to the presence of any ice. Thus, it is less likely to underestimate thin ice than the other algorithms. Due to this sensitivity to thin ice, which is common in the marginal ice zone (a region of substantial operational interest) Cal/Val replaced NASA Team as the operational algorithm at the NIC. However, this high sensitivity causes the algorithm to saturate quickly to 100% ice concentration and results in truncation of Cal/Val concentration estimates to 100%. Thus, while the Cal/Val may be more accurate at detecting thin ice, the algorithm is prone to overestimate ice concentration in regions of thicker ice. The Cal/Val has now been replaced by NASA Team 2 as the operational algorithm at NIC.

### C. NASA Team

The NASA Team algorithm was originally developed for the SMMR instrument [26] and was later adapted for SSM/I [27]. It uses two ratios, a polarization ratio (horizontal and vertical channels of 19 GHz) and a gradient ratio (the vertical polarization of 19 and 37 GHz). The use of ratios reduces the dependence of the retrieved concentrations on surface temperature. The ratios can be used to infer three surface types: water, and two ice types that roughly correspond in the Arctic to first-year ice (ice that has not survived a melt season) and multiyear ice (ice that has survived at least one melt season). In the present paper, only total ice concentration is evaluated.

The NASA Team algorithm is particularly sensitive to the error introduced by thin ice (e.g., [9]). A thin ice modification was made to the algorithm for such regions [28] such that the two ice types correspond roughly to first-year ice and thin ice; however, in this study, we examined only the standard NASA Team algorithm, without the thin ice modification.

Despite these limitations, the NASA Team algorithm is robust and has been widely used within the science community. It is one of the two sea ice concentration products archived at the NSIDC. Most of the long-term sea ice trends have been studied using the NASA Team algorithm. The algorithm has also been commonly used in operational analyses.

### D. NASA Team 2

The NASA Team 2 algorithm [29] is an enhanced version of the original NT algorithm and is formulated in a similar manner. The N2 algorithm is distinct from the other three algorithms in that it employs the 85-GHz channels. Historically, the 85-GHz channels were deemed too susceptible to atmospheric emission to be useful for automated sea ice retrievals. The atmosphere emits much more strongly at 85 GHz than at 19 and 37 GHz, especially when optically thick clouds are present. The N2 algorithm corrects for this atmospheric contribution via a simple forward radiative transfer model. Over each pixel, the model is run for 11 typical polar atmospheres. The closest match to the raw 85-GHz brightness temperature is selected and used to correct the raw values and provide a clear-sky 85-GHz brightness temperature.

The 85-GHz channels can complement the 19- and 37-GHz channels and provide additional information for estimating ice concentration. Also, at the 85-GHz frequency, emission comes primarily from the snow or ice surface. Thus, the 85-GHz channels are less sensitive to inhomogeneities in the snow or ice (particularly icy, refrozen layers within the snow) [29]. Because of these advantages, the NASA Team 2 algorithm has now replaced the Cal/Val as the Arctic operational algorithm at the NIC and is the standard AMSR-E concentration product. Other passive microwave ice concentration algorithms using 85-GHz information (e.g., [30]–[33]) have also been developed, but they have been applied only to specific regions or seasons or require interactive tiepoint selection and/or specific atmospheric information (such as from a numerical weather prediction model).

### E. Weather Filter

As mentioned above, atmospheric emission can make a significant contribution to the signal received by the sensor. Because the microwave emission from the ocean surface is much lower than from sea ice, the atmosphere is generally a larger factor over the ocean. Increased emission over the water, either from increased liquid water or water vapor in the atmosphere or wind roughening of the ocean surface can result in brightness temperatures comparable to sea ice in these areas [27]. Wind roughening can affect open ocean regions near the ice edge or water within the ice pack—in leads or polynyas. Horizontally

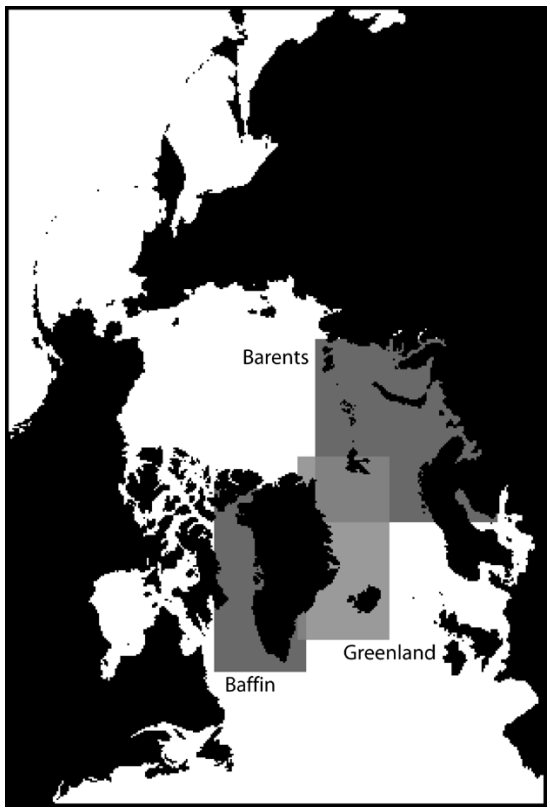


Fig. 1. Map of Arctic region on the NSIDC polar stereographic grid with Baffin Bay, Barents Sea, and Greenland Sea regions specified. Note that some of the Greenland Sea region overlaps with the Baffin and Barents regions.

polarized channels are typically more affected by wind roughening than vertically polarized channels [20].

To alleviate these effects, two weather filters were developed to screen out erroneous retrievals over the ocean. The first uses a cutoff value of the NASA Team 19- and 37-GHz gradient ratio [34]. An additional filter was later developed using a gradient ratio of the 22- and 19-GHz frequencies [35]. If either gradient ratio exceeds the prescribed value, the pixel is set to zero concentration. The result is to generally cut off ice concentrations below 15%, which eliminates most spurious open ocean ice retrievals. While initially developed for the NASA Team algorithm, for consistency these filters have been employed with all four algorithms discussed here; in this study, the selected regions avoid most open ocean areas, so the effect of the weather filters is not significant.

## V. AVHRR Imagery

The SSM/I-derived ice concentration products are evaluated in this study through comparisons with imagery from the NOAA Advanced Very High Resolution Radiometer (AVHRR). AVHRR is a sun-synchronous polar-orbiting sensor, with five channels spanning visible and infrared portions of the electromagnetic spectrum. AVHRR scenes were obtained from the Danish Meteorological Institute (DMI) in Copenhagen, Denmark. Imagery was obtained from three regions in the Arctic that are adjacent to the North Atlantic. The regions are denoted in this study as: 1) Baffin Bay; 2) the Greenland Sea; and 3) the Barents Sea (Fig. 1). These regions were selected for availability of AVHRR imagery from DMI, their importance to operational activities, and for the variety of surface conditions generally present. The regions actually encompass larger areas than their names imply (e.g., the Baffin Bay region includes the northern part of the Labrador Sea and the Barents Sea includes the Kara and northern Baltic Sea), but the comparisons in this study focus on sea ice only in the three specific named areas of the regions. Also note that the regions overlap in some areas, particularly the Barents and Greenland regions in the Fram Strait area. When the overlap region was clear sky, it was only analyzed in one of the regions (the one with the largest clear-sky area).

All three regions encompass the ice edge over much of the year. Baffin Bay ice cover is almost exclusively seasonal in nature (i.e., first-year ice), and the region melts out completely during the summer. First-year ice also dominates the Barents Sea, with multiyear ice in the north. Both the Baffin and Barents regions have substantial ice growth during the fall freeze-up period and melt during the summer. The Greenland Sea region is dominated by multiyear ice floes exiting the Arctic basin through Fram Strait. However, the Greenland Sea region can also contain regions of intense new ice growth in winter.

The AVHRR's instantaneous field of view varies with scan angle, with a nadir ground resolution of about 1.1 km. The imagery used here was mapped onto the same NSIDC polar stereographic projection as the SSM/I ice concentrations, with a gridded resolution of 2.5 km. Thus, one $25 \times 25$ km SSM/I pixel contains 100 ($10 \times 10$) AVHRR pixels. Spatial resolution (instantaneous field of view) of AVHRR decreases off-nadir, so some AVHRR pixels near the image edge may be interpolated. However, the use of a lower resolution grid than the nominal nadir resolution results in oversampling for most pixels in the AVHRR scenes.

Several AVHRR scenes of Channel 2 (0.72–1.1 $\mu$m) or Channel 4 (10.3–11.3 $\mu$m) imagery were collected daily from each region for a summer period (June 2001–August 2001) and a winter period (November 2001–March 2002). Many scenes were almost completely cloud-covered and thus of limited use for comparison with the SSM/I sea ice concentrations. In each region, one image from each day with substantial clear sky was used for the comparisons; images were collected at roughly the same time of day (midmorning) if possible. Seventeen scenes from the summer period and 31 scenes from the winter period contained substantial areas of clear sky. The cloud-free regions within each AVHRR scene were selected by visual inspection using image display software. While we cannot say how representative the selected scenes are of the general conditions within each region, the scenes encompass a variety of ice conditions and thus provide at least a general indication of conditions that might be encountered throughout the year. Table II lists the region, date, and the number of corresponding 25-km resolution pixels for each AVHRR scene used in this study.

## VI. AVHRR Ice Concentration

Similar to Comiso and Steffen [6], ice concentration was derived from AVHRR imagery using two methods, depending on

TABLE II
SUMMARY OF SCENES FOR EACH SEASON WITH REGION, DATE, AND NUMBER OF CORRESPONDING 25-km RESOLUTION SSM/I PIXELS

| *Scene #* | *Summer* | | | *Winter* | | |
|---|---|---|---|---|---|---|
| | Region | Date | # pixels | Region | Date | # pixels |
| 1 | Baffin | 06/15 | 134 | Baffin | 12/17 | 387 |
| 2 | Baffin | 06/16 | 84 | Baffin | 02/10 | 264 |
| 3 | Baffin | 06/28 | 246 | Baffin | 02/11 | 331 |
| 4 | Baffin | 07/03 | 158 | Baffin | 02/27 | 228 |
| 5 | Baffin | 07/11 | 155 | Baffin | 03/04 | 312 |
| 6 | Barents | 06/16 | 279 | Baffin | 03/24 | 305 |
| 7 | Barents | 06/16 | 686 | Baffin | 03/28 | 291 |
| 8 | Barents | 07/05 | 328 | Baffin | 03/30 | 268 |
| 9 | Barents | 07/17 | 196 | Barents | 12/25 | 269 |
| 10 | Barents | 07/21 | 230 | Barents | 01/20 | 292 |
| 11 | Barents | 07/24 | 221 | Barents | 01/23 | 681 |
| 12 | Barents | 08/02 | 133 | Barents | 01/25 | 226 |
| 13 | Barents | 08/09 | 247 | Barents | 01/29 | 233 |
| 14 | Barents | 08/23 | 350 | Barents | 02/05 | 279 |
| 15 | Greenland | 06/23 | 240 | Barents | 03/11 | 287 |
| 16 | Greenland | 06/27 | 272 | Barents | 03/22 | 292 |
| 17 | Greenland | 07/02 | 166 | Barents | 03/26 | 392 |
| 18 | | | | Greenland | 11/12 | 145 |
| 19 | | | | Greenland | 12/21 | 337 |
| 20 | | | | Greenland | 12/24 | 243 |
| 21 | | | | Greenland | 12/29 | 215 |
| 22 | | | | Greenland | 01/20 | 135 |
| 23 | | | | Greenland | 01/23 | 461 |
| 24 | | | | Greenland | 01/25 | 374 |
| 25 | | | | Greenland | 01/29 | 321 |
| 26 | | | | Greenland | 02/18 | 374 |
| 27 | | | | Greenland | 02/27 | 285 |
| 28 | | | | Greenland | 03/05 | 353 |
| 29 | | | | Greenland | 03/18 | 426 |
| 30 | | | | Greenland | 03/19 | 454 |
| 31 | | | | Greenland | 03/24 | 312 |

the season. Other evaluations of passive microwave ice concentrations using visible and infrared imagery have employed a similar methodology (e.g., [11], [12], [36], and [37]). During summer, surface temperatures of ice and water are near freezing and surface albedo best distinguishes ice and water, as indicated by AVHRR Channel 2 (0.72–1.1 $\mu$m) reflectance. In winter, when there is very limited solar illumination, ice can be discriminated from water by its lower surface temperature, as indicated by AVHRR Channel 4 thermal infrared (10.3–11.3 $\mu$m) radiance. Thus, a threshold method (a pixel is either 100% ice or 100% water) from Channel 4 is used during winter and a mixing method (a pixel has an ice concentration of 0% to 100%) from Channel 2 is used during summer. The details of these two methods are provided in the following paragraphs.

In winter, ice growth is common in the three regions. As the surface temperature falls below the ocean freezing temperature ($\sim 271$ K), sea ice begins to form. As ice thickens, the surface temperature, indicated by the Channel 4 brightness temperature, will decrease. Thus, temperatures below $\sim 271$ K indicate ice and temperatures above $\sim 271$ K indicate water and a threshold method can be used. Any pixel with a temperature below the ocean freezing point ($\sim 271$ K) was deemed to be ice and given a concentration of 100%. A pixel with a temperature above the freezing point was given a concentration of 0%. This method assumes that pixels do not contain a mixture of ice and water, which introduces some error into the AVHRR winter ice concentrations. This error is particularly relevant for pixels containing many small floes. Such pixels may have values below the threshold and be counted as ice despite the fact that they contain substantial open water. This leads to a tendency for the threshold method to overestimate ice concentration. However, this error is generally small compared to the errors in the SSM/I concentrations [36].

Sensor angle, atmospheric emission, and local surface conditions can affect the retrieved Channel 4 brightness temperature. To minimize errors, individual thresholds were determined for each AVHRR scene in the same region (see Fig. 1) where the comparisons were conducted. The thresholds were selected using image enhancement techniques such as contrast stretching to be as accurate as possible. A threshold was computed from a small, representative region near the ice edge, but where no ice was apparent. The mean threshold value was then lowered by one standard deviation (of the all the points in the representative region) to account for noise and local variability in the AVHRR signal, similar to the methodology of Comiso and Steffen [6]. The result is that some open water pixels may be misclassified as ice, but there is a lower likelihood of missing ice. The regions of AVHRR imagery were selected to avoid large open water areas, so such errors should be small.

During summer, there is primarily ice melt, with little or no ice growth. The Channel 2 reflectance for a pixel is indicative of the proportion of water and ice in that pixel. Thus, the concentration for each pixel can be determined from an interpolation between pure ice and pure water tiepoints. Reflectance also varies based on sun angle, sensor angle, and ice conditions (e.g., melt). To reduce these errors, imagery was collected from approximately the same time of day and tiepoints were independently chosen for each image so that the effects of changes in sensor and sun angle were minimized. A group of pure open water and pure ice pixels were manually selected using image enhancement techniques from the same region as the comparison with the SSM/I ice concentrations (see Fig. 1). The ice pixels were selected from the middle of a large floe representative of the surrounding ice conditions to assure, as much as possible, an accurate 100% ice tiepoint. As with the threshold method, the mean tiepoint values were adjusted by one standard deviation (lower reflectance for the ice tiepoint and higher reflectance for the water tiepoint) for to account for noise, sensor and sun angle, and surface variability.

After the AVHRR ice concentrations were computed on the 2.5-km imagery, the concentration fields were binned via a drop-in-the-bucket method to the SSM/I 25-km grid resolution. (If there were any missing pixels in the AVHRR 2.5-km grid, these were not used in the rebinning.) This allows a pixel-to-pixel comparison with the SSM/I concentration fields on a consistent grid.

## VII. DISCUSSION OF ERROR SOURCES

Comiso and Steffen [6] estimate an error in visible/infrared ice concentrations to be 5% to 20%. Other evaluations have found similar AVHRR error in comparisons with other imagery such as Landsat; for example, Emery *et al.* [36] found root mean square (RMS) errors ranging between 6.8% and 15.1% in summer (tiepoint method) and between 8.6% and 26.8% in winter (threshold method). However, Emery *et al.* did not calculate tiepoints/thresholds for each scene; Comiso and Steffen

TABLE III
CHANGE IN AVHRR WINTER ICE CONCENTRATION (PERCENT) FOR GIVEN CHANGE IN WATER/ICE THRESHOLD. ROW 1 IS THE MEAN CHANGE IN CONCENTRATION FOR EACH $1\sigma$ CHANGE IN THRESHOLD VALUE. ROW 2 IS THE RANGE OF THE 95% CONFIDENCE LEVEL. ROW 3 IS THE LARGEST MAGNITUDE (POSITIVE MAXIMUM OR NEGATIVE MINIMUM) CHANGE. THE AVHRR IMAGERY IS INVERTED SO AN INCREASE IN THE THRESHOLD VALUE DECREASES ICE CONCENTRATION

| | $-2\sigma$ | $-1\sigma$ | $+1\sigma$ | $+2\sigma$ |
|---|---|---|---|---|
| Avg. $\Delta$ | 1.1 | 0.6 | -0.9 | -2.0 |
| 95% range | ±2.2 | ±1.4 | ±2.2 | ±5.2 |
| Max or Min | 5.9 | 4.1 | -5.4 | -11.4 |

TABLE IV
CHANGE IN AVHRR SUMMER ICE CONCENTRATION (PERCENT) FOR GIVEN CHANGE IN WATER AND ICE TIEPOINTS. ROW DESCRIPTIONS ARE THE SAME AS IN TABLE II. VALUES CALCULATED INDEPENDENTLY FOR ICE AND WATER TIEPOINTS

| | *Water* | | | | *Ice* | | | |
|---|---|---|---|---|---|---|---|---|
| | $-2\sigma$ | $-1\sigma$ | $+1\sigma$ | $+2\sigma$ | $-2\sigma$ | $-1\sigma$ | $+1\sigma$ | $+2\sigma$ |
| Avg. $\Delta$ | 1.0 | 0.5 | -0.6 | -1.3 | 3.2 | 1.6 | -1.9 | -3.9 |
| 95% | ±2.6 | ±1.4 | ±1.6 | ±3.6 | ±3.8 | ±2.2 | ±2.2 | ±4.6 |
| Max or Min | 4.3 | 2.4 | -2.8 | -6.5 | 7.2 | 3.9 | -4.3 | -8.8 |

estimate that with careful selection of tiepoints/thresholds the error is expected to be smaller $(< 5\%)$ in consolidated ice regions with dry surface conditions.

A large part of the potential error is due to the fact that there is some subjectivity in the selection of the thresholds and tiepoints. To assess the impact of their selection on the calculated AVHRR ice concentrations, a sensitivity study was conducted. The calculated thresholds and tiepoints used to calculate the AVHRR ice concentration were adjusted by $\pm 1$ or $\pm 2$ standard deviations (typically 5% to 10% of the original tiepoint/threshold value), based on the group of pixels used to compute the original tiepoints/thresholds. The ice concentrations appear to be relatively insensitive to changes in the thresholds (Table III) and tiepoints (Table IV), with average concentration (over an entire AVHRR scene) changes mostly less than 2%, 95% confidence levels (variation around the average change in concentration, $\Delta$) generally between 2% to 5%, and maximum changes in ice concentration for an AVHRR scene generally less than 10%. Thus, for the cases presented here, it appears that AVHRR errors are likely on the lower end of the estimates by Comiso and Steffen and others.

Even with careful selection of AVHRR tiepoints and thresholds, there are several sources of error that could affect the SSM/I–AHVRR concentration comparisons. Here we briefly discuss error sources for the AVHRR and SSM/I concentrations. More information can be obtained in the accompanying references cited.

Analysis regions were interactively selected in the collocated AVHRR and SSM/I concentration fields using image analysis software. The regions were selected conservatively to include, as much as possible, only unambiguous clear sky areas. However, thin cirrus clouds may be present in some areas and could introduce some error into the AVHRR concentrations. Because cirrus clouds may have a temperature and albedo similar to ice and because the ice surface may still be visible through them, they may be difficult to detect by visual inspection. Automated detection methods could be employed to screen out clouds. However, these methods have limitations, and for this study manual inspection was deemed more appropriate. The effect of cirrus clouds on AVHRR ice concentration estimates depends on the thickness, albedo, and temperature of the cloud and may result in either an overestimation or underestimation of ice concentration, depending on conditions. Low-level clouds and fog may also occur over open water, thin ice, or melting ice regions and can lead to misidentification because they may have similar temperature or albedo signatures as the surrounding ice. However, these are more easily detected than cirrus clouds because of texture contrast between the clouds and the ice.

Because of SSM/I's field of view is larger than the gridded pixel resolution, pixels adjacent to land may include emission from the land. To avoid errors from land contamination, regions were selected to be at least two pixels from land in the SSM/I concentrations. Selected regions also often included the ice edge, but were chosen to avoid most open water areas. This eliminated areas where the SSM/I fields are weather filtered and the concentrations are prescribed to be 0%, which prevents the statistics from being unrealistically improved due to the inclusion of large regions of open water. The weather filters are subject to errors as well, and even with the filters, false ice can be retrieved many kilometers off the ice edge. Because this study does not cover most open water areas, such errors are not directly addressed, although errors from the weather filter could also potentially affect retrievals at the ice edge to some extent.

In addition to the potential errors induced by clouds in the AVHRR concentrations and land contamination in SSM/I concentrations, there are several other sources of error. A major potential source of error in the SSM/I concentrations is the use of hemispheric tiepoints. These unchanging tiepoints may not be representative of conditions at a specific time and place.

The SSM/I concentrations are computed on daily composites of brightness temperatures, with the larger footprint of the individual SSM/I channels averaged onto a 25-km resolution grid. This will result in errors from both temporal and spatial averaging of the brightness temperatures. Additionally, since the AVHRR images are snapshots at a specific time, some of the difference between the AVHRR and SSM/I concentrations may be due to changing ice conditions during the 24-h period.

The surface emission of microwave energy varies depending on the medium. Since the SSM/I algorithms use different combinations of channels, the effects of these surface variabilities will be different for each algorithm. The NASA Team and NASA Team 2 algorithms use brightness temperature ratios. Thus, these two algorithms are less sensitive to the physical temperature of the surface than the Bootstrap and Cal/Val algorithms, which do not use ratios. The NASA Team algorithm uses the 19 V, 19 H, and 37 V channels, while the Bootstrap algorithm uses the 19 V, 37 V, and 37 H channels. This leads to different sensitivities of the algorithms to the surface characteristics, as discussed in detail in Comiso *et al.* [10].

The Cal/Val algorithm uses either a combination of the 19 V and 37 V (within the ice pack) or the 37 V and 37 H channels (near the ice edge to potentially yield a more precise edge location by employing only the smaller footprint 37-GHz channels). Of particular note, the Cal/Val's tiepoints are set to be

very sensitive to the presence of ice. Thus, the Cal/Val more readily detects thin ice. However, because of the high sensitivity, in the presence of thicker ice, it quickly saturates to 100% ice. Thus, small variability in high concentration regions is missed and there is a tendency for the Cal/Val to overestimate concentration [9], [38].

Because the NASA Team 2 algorithm employs the 85-GHz channels, it is potentially more susceptible to atmospheric contamination than the other algorithms. While the inverse radiative transfer model corrects for atmospheric influence, errors could remain if the conditions do not correspond to one of the 11 standard atmospheres used by the model. On the other hand, the additional information provided by 85-GHz channels can reduce uncertainties that occur in the other algorithms.

## VIII. Statistical Results

In this study, we compare the four SSM/I algorithms using AVHRR concentrations as the basis for comparison. In this sense then, AVHRR acts as a "true" concentration with which to compare the SSM/I estimates. However, while AVHRR concentrations are expected to be much more accurate than those from SSM/I, there are several sources of error in the AVHRR fields (as noted above). Thus, when "error," "bias," and "error standard deviation" are used below, these error terms should be considered as "SSM/I error relative to AVHRR," etc. Below, statistical analyses are presented based on overall summary results of all pixels in all scenes, then based on breakdowns by season, region, ice conditions, and finally individual scene. Confidence levels are also computed to assess the significance of the differences between the errors of the SSM/I algorithms.

### A. Overall Summary Statistics

*1) Mean Error:* The overall mean error (bias) of SSM/I concentrations relative to AVHRR (from all pixels in all scenes) agrees with previous studies (e.g., [9]–[12]). Both BT and NT underestimate total concentration, but NT has a larger bias (Table V). CV overestimates total concentration due to the oversensitivity to the presence of ice, but the bias is much smaller than NT and BT. Like the NT, the N2 algorithm underestimates concentration, but the magnitude is much smaller. In fact, the N2 concentration biases are smallest of the four algorithms.

Breaking the statistics into seasonal components (Table V) yields the same relative biases between the algorithms (although the difference between winter N2 and CV bias magnitudes is not significant), but the summer magnitudes are larger (as expected due to surface melt and increased atmospheric moisture). The CV bias increases (becomes more positive) in the summer, while the bias of the other algorithms decrease (becomes more negative). This is likely due to the tendency of CV to saturate and overestimate concentration. Essentially this means that CV has a tendency to interpret the microwave signal of broken floes of thick ice in a pixel as completely ice covered. As discussed further below, the CV summer overestimation occurs in the Greenland and Barents Seas, which in the summer are characterized by a mixture of open water and thick multiyear floes.

TABLE V
Summary Statistics of SSM/I Ice Concentration Error (Percent) Relative to AVHRR; in Parentheses Below Are the 95% Confidence Level Ranges. Values in Bold Have the Lowest Magnitude (Nearest to Zero for the Mean Difference) and Are Statistically Significant From the Other Algorithm Errors at the 95% Level. In the Right Columns, Both Error st. Dev. and RMS Error Are Present; the Confidence Levels Were Computed Based on the Error St. Dev.

| | # 25 km pixels | *Mean* | | | | *St. Dev./RMS* | | | |
|---|---|---|---|---|---|---|---|---|---|
| | | BT | CV | N2 | NT | BT | CV | N2 | NT |
| Total | 13897 | -5.3 (±0.2) | 1.8 (±0.2) | **-1.2** (±0.2) | -9.0 (±0.2) | **12.9**/13.9 (±0.4) | 13.9/14.0 (±0.4) | 13.7/13.8 (±0.6) | 14.6/17.2 (±0.4) |
| Summer | 4125 | -6.1 (±0.4) | 4.3 (±0.6) | **-2.6** (±0.4) | -10.5 (±0.4) | 14.6/15.8 (±0.4) | 16.9/17.4 (±1.0) | 15.7/15.9 (±1.2) | 15.9/19.1 (±1.2) |
| Winter | 9772 | -5.0 (±0.2) | 0.7 (±0.2) | -0.6 (±0.2) | -8.4 (±0.2) | 12.2/13.2 (±0.4) | 12.3/12.3 (±0.6) | 12.7/12.7 (±0.6) | 13.9/16.2 (±0.4) |

To assess the significance of the differences between the errors of the four SSM/I algorithms, confidence levels were calculated using a type of Monte Carlo simulation, called a bootstrap method [39] (not to be confused with the Bootstrap ice concentration algorithm). The original $N$ sample dataset is replaced by $N$ random samples of the dataset. Thus, the size of the data is the same ($N$), but the replacement dataset will use some data points multiple times and other data points will be omitted. One thousand replacement datasets were created to estimate the significance of the original estimates. This procedure allows one to assess whether the differences between the errors of the different algorithms are likely real (i.e., significant) or may be an artifact of the statistical sampling (not significant). In this study, the mean errors of the SSM/I algorithms (relative to AVHRR) are statistically different from each other at the 95% significance level except for the winter CV and N2 estimates (Table V).

*2) Error Standard Deviation:* Two commonly used standard statistical measures of uncertainty are error standard deviation (SD) and RMS error. The RMS error includes the bias as part of its uncertainty estimate, while error SD is a measure of the uncertainty without the bias. Because some of the biases in this study are quite large in some instances, the RMS error estimate can be notably different than the error standard deviation. In some sense, the RMS error is a better measure of the true uncertainty because it includes the bias. However, here we focus on the error SD so that the bias and uncertainty can be discussed independent of each other. For comparison, RMS errors are listed alongside the error SD in Table V.

The BT algorithm has the lowest error standard deviation relative to AVHRR (Table V) overall and in the seasonal breakdowns, but only in the overall case is it significantly different from the other algorithms at the 95% level. In general, the error SD for all four SSM/I algorithms are quite similar, varying between 12% and 17%. The RMS error values show a similar range (12% to 19%), with the primary difference being that the BT algorithm in the overall case no longer has the lowest uncertainty to a statistically significant (95%) level (due to the higher bias of BT compared to CV and N2).

In theory, spatial resolution can potentially have an effect on the retrieved concentration in the selection of frequencies used by a given algorithm. Since the SSM/I footprint is a function of frequency, the combination of channels used by the algorithm also influences the effects of resolution: the 37-GHz footprint is

TABLE VI
SSM/I ICE CONCENTRATION ERROR ST. DEV. FOR 2.5-km GRID AND 25-km GRID (PERCENT)

| Grid Resolution | BT | CV | N2 | NT |
|---|---|---|---|---|
| 2.5 km | 20.5 | 20.6 | 20.7 | 21.2 |
| 25 km | 12.9 | 13.9 | 13.7 | 14.6 |

substantially smaller than the 19-GHz footprint. Thus, it may seem counterintuitive that Cal/Val, which uses only 37-GHz channels near the ice edge, does not show significantly less uncertainty than the other algorithms (which use both 19- and 37-GHz channels). This is likely because the information lost by not using the 19-GHz frequencies and the greater potential atmospheric influence of the 37 H channel offsets any gains from using only higher resolution channels.

The lack of significant differences between the error standard deviations indicates that the uncertainties of the SSM/I concentration estimates are not fundamentally related to the choice of algorithm, but are primarily a function of factors common to all four algorithms, with the most likely major factor being the spatial resolution. The SSM/I brightness temperatures are a function of the emissivity over the entire grid cell (actually a region larger than the grid since the sensor footprint is larger than the gridded resolution). Particularly in this study, where pixels near the ice edge are used, the brightness temperature signal is an average of several different surface types over each pixel. This signal is not necessarily unique, but rather may come from several possible mixtures of surface types. While each algorithm takes different approaches, all are limited by this fact, and we believe this is an important reason why the uncertainties of the algorithm estimates are not significantly different from each other. With higher resolution, the passive microwave algorithms would more likely see pure ice types or less ambiguous mixtures of ice types and differences between the algorithm uncertainties may be more apparent.

While this issue cannot explicitly be explored here, we attempt to illustrate the role of spatial resolution by scaling the 25-km SSM/I concentrations (without interpolation) to the same 2.5-km resolution as in the original AVHRR and conducting a pixel-to-pixel comparison at the 2.5-km resolution. While the mean errors are virtually unchanged, the error SDs are much larger (Table VI). This is because, while the SSM/I's effective gridded spatial resolution does not change (still 25 km), the AVHRR retrieves much more spatial detail, leading to an increased error SD when comparing the two. This does not imply anything about the individual algorithm uncertainties relative to AVHRR because the only valid comparison is at the nominal 25-km gridded resolution of SSM/I. However, it does illustrate that the pixel is representative of a spatial average. Thus, the uncertainty at a given location or subpixel region within a pixel may be much larger. This has significant ramifications when using SSM/I-retrieved ice concentrations at an operational scale or in determining the ice edge.

### B. Statistics by Region

The statistics are also broken down by region within each season (Tables VII and VIII). While these regional results generally agree with the overall and seasonal statistics, there are some exceptions, particularly in the mean differences. In the Baffin Bay during summer, CV actually underestimates concentration, probably due to the extreme melting (although the underestimation is much less than NT or BT). In Greenland during summer, the N2 overestimates concentration and the underestimations by BT and NT are smaller, perhaps due to the infusion of multiyear floes through Fram Strait. The situation is reversed in Greenland in the winter, with all algorithms, even CV, underestimating concentration, although the CV's bias is quite small (particularly compared to BT and NT). This is likely due to an increased proportion of thin ice (from winter ice growth) relative to multiyear ice compared to summer; because CV is better able to detect the thin ice, its bias is smallest. Significance tests for the regional statistics and the statistics by ice condition (below) are similar to those for the overall summary statistics and are not included here.

TABLE VII
SUMMER REGIONAL BREAKDOWN OF SSM/I ICE CONCENTRATION ERROR (PERCENT)

| Region | # 25 km pixels | *Mean* | | | | *St. Dev./RMS* | | | |
|---|---|---|---|---|---|---|---|---|---|
| | | BT | CV | N2 | NT | BT | CV | N2 | NT |
| Baffin | 777 | -14.6 | -1.4 | -7.6 | -13.4 | 13.5/19.9 | 14.7/14.8 | 13.4/15.4 | 14.9/20.0 |
| Barents | 2670 | -4.4 | 4.7 | -2.7 | -11.3 | 13.6/14.3 | 17.3/17.9 | 15.7/15.9 | 15.6/19.3 |
| Greenland | 678 | -3.2 | 9.0 | 3.6 | -4.2 | 15.9/16.2 | 16.0/18.4 | 16.2/16.6 | 16.9/17.4 |

TABLE VIII
WINTER REGIONAL BREAKDOWN OF SSM/I ICE CONCENTRATION ERROR (PERCENT)

| Region | # 25 km pixels | *Mean* | | | | *St. Dev./RMS* | | | |
|---|---|---|---|---|---|---|---|---|---|
| | | BT | CV | N2 | NT | BT | CV | N2 | NT |
| Baffin | 2386 | -2.8 | 1.9 | 0.1 | -4.3 | 12.1/12.4 | 12.3/12.4 | 12.1/12,1 | 12.5/13.2 |
| Barents | 2951 | -3.4 | 1.8 | 0.3 | -4.1 | 11.1/11.6 | 11.2/11.3 | 12.2/12.2 | 13.9/14.5 |
| Greenland | 4435 | -7.3 | -0.6 | -1.5 | -13.4 | 12.5/14.5 | 12.9/12.9 | 13.2/13.3 | 12.8/18.5 |

TABLE IX
SSM/I ICE CONCENTRATION ERROR (PERCENT) FOR AVHRR CONCENTRATION RANGES

| AVHRR Conc. Range (%) | # 25 km pixels | *Mean* | | | | *St. Dev./RMS* | | | |
|---|---|---|---|---|---|---|---|---|---|
| | | BT | CV | N2 | NT | BT | CV | N2 | NT |
| 90-100 | 10639 | -7.3 | -1.2 | -4.0 | -11.7 | 8.9/11.5 | 7.8/7.9 | 7.8/8.8 | 10.1/15.5 |
| 0-90 | 3258 | 0.9 | 11.5 | 7.9 | -0.3 | 20.1/20.1 | 22.6/25.4 | 22.3/23.7 | 21.7/21.7 |
| 50-100 | 13228 | -6.6 | 0.5 | -2.7 | -10.6 | 10.7/12.6 | 11.3/11.3 | 10.4/10.7 | 11.5/15.6 |
| 0-50 | 669 | 19.9 | 26.9 | 28.7 | 22.4 | 23.1/30.5 | 29.5/39.9 | 28.7/40.6 | 27.1/35.2 |

### C. Statistics by Ice Condition

The heterogeneity of the ice pack is a major factor in the accuracy of the SSM/I algorithm, as mentioned above in the discussion of the effect of spatial resolution. To investigate this further, statistics were computed based on the compactness of the ice pack, based upon 90% and 50% AVHRR concentration thresholds (Table IX). Most pixels are in more compact ice conditions, partially due to the criteria of the region selection to avoid large regions of open water; it is also due to the general ice conditions in the region—where ice exists it tends to be compact, especially in winter. In more compact ice conditions ($> 90\%$ and $> 50\%$), biases and RMS differences are much lower than in regions with sparse ice. In these regimes, CV performs particularly well, with the smallest bias and small standard deviations. Of note is that fact that all four SSM/I algorithms estimate lower concentrations than AVHRR (negative bias) in the 90% to 100%

regime. While this may reflect underestimation by SSM/I, some of the negative bias may also be indicative of overestimation by AVHRR. The tiepoint/threshold selection criteria for AVHRR (discussed in Section VI) are conservative so as not to miss any ice. However, this leads to the potential to saturate and possibly overestimate high concentrations.

In the areas of sparsest ice, the $< 50\%$ regime, N2 has the largest bias, but all algorithms overestimate concentration by a substantial amount—even BT and NT, despite their penchant to underestimate concentration. Because many of the pixels in this regime may encompass the ice/water boundary, the atmospheric influence may have an effect, particularly on the N2 estimates. Another contributor to the higher errors is the spatial resolution of SSM/I. The samples in the $< 50\%$ regime are often very close to the ice edge (within one or two pixels). The sensor footprint of SSMI (69 km $\times$ 43 km for 19 GHz) is larger than the gridded resolution and a 25-km pixel that is open water or very low concentration in AVHRR may show substantial ice in the same pixel of the SSM/I concentration because information from tens of kilometers into the ice pack is included. This results in the potential for SSM/I to overestimate ice concentration at the ice edge and illustrates that SSM/I's ability to precisely determine ice edge location is limited. Again, the main contributor to this ice edge error is the low spatial resolution of the sensor. Use of 85-GHz imagery could potentially yield a more precise ice edge (e.g., [31]), but it again is limited by atmospheric influences. This study does not address the precision of the ice edge in any further detail. However, it is important to operational activities and previous studies (e.g., [9]) have shown large (10–100 km) discrepancies in the location of the ice edge from SSM/I.

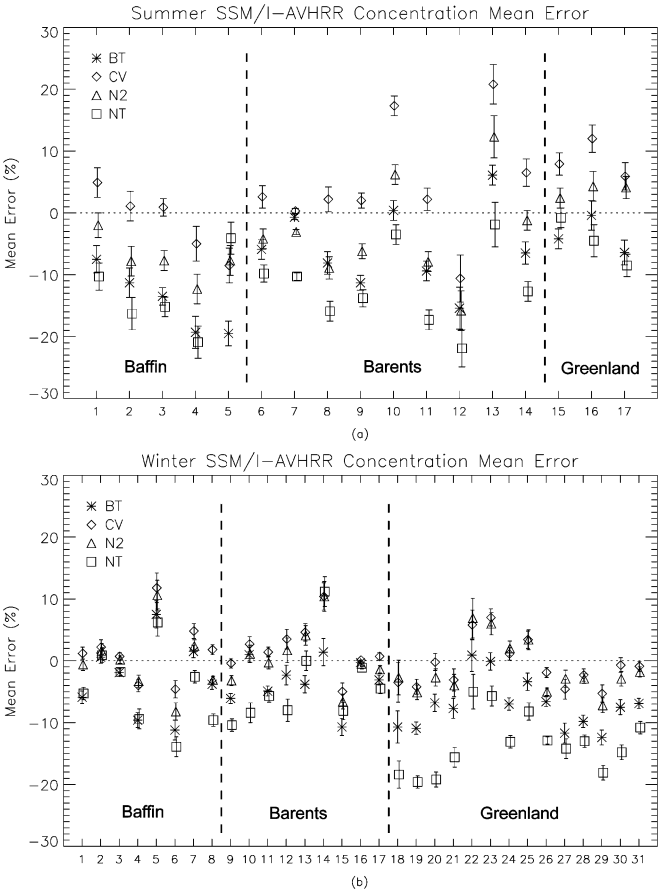


Fig. 2. Mean error of SSM/I-derived concentrations relative AVHRR concentrations (in percent) for (a) summer and (b) winter. The $x$ axis is the scene number as provided in Table II. Error bars represent the range of the 95% confidence level, as calculated using a bootstrap method.

### D. Scene-by-Scene Statistics

To demonstrate the variation of the SSM/I algorithm errors, mean error and error SD are computed for each scene (Figs. 2 and 3), along with confidence levels computed with the Monte Carlo bootstrap method. These generally reflect the summary results. The SSM/I algorithms tend to underestimate ice concentration, except for CV. The underestimation is particularly pronounced in the NT estimates. The underestimations are larger in summer than in winter. There also tends to be more uncertainty in the summer mean error estimates. However, in both summer and winter, at least one algorithm, and often all four, have mean errors that are significantly different from each other at the 95% confidence level.

Of particular note, there is a great deal of variation in the mean errors of the SSM/I ice concentrations from scene to scene. From day to day, any of the four algorithms may have the lowest difference. Thus, while N2 has the smallest bias on average (Table V), CV, BT, and even occasionally NT, may have the least bias in a given scene.

Conversely, the error SDs of the algorithms are only rarely significantly different from each other at the 95% level (Fig. 3), consistent with the overall and seasonal results. Daily RMS errors (not shown) show similar variability and also indicate that the algorithms rarely have significantly different values. As with the means, summer error SD values are slightly larger than in winter. And like the mean differences, the error SDs show a great deal of variation from scene to scene—on any given day any one of the algorithms may perform best. While on many days, most or all of the algorithms fall within each other's 95% significance levels, there are days where one algorithm is clearly best. Summer Scene 13 is a notable example. The AVHRR imagery indicates a very diverse ice cover with many small floes of differing character. In this case, BT is clearly superior with the lowest error SD and a much narrower significance range.

## IX. Case Studies

To further illustrate the differences between the passive microwave algorithms, two case studies are presented. The first is a summer case in the Barents Sea on June 16, 2001 and consists of summer scenes 6 and 7 (Table II). The second is a winter case in the Greenland Sea on February 27, 2002 (Winter Scene 27). The full AVHRR images with outlines of the region of each case study outlined in white are provided in Fig. 4. While the AVHRR concentration fields were coarsened from 2.5 to 25 km for statistical comparison with SSM/I, in the case study images the AVHRR fields are left in their original 2.5-km resolution to illustrate their greater spatial detail.

### A. Summer—Barents Sea, June 16, 2001

In the comparisons, one AVHRR scene per day was acquired for comparison with SSM/I and in most cases the clear sky region of the scene was examined as one entity. However, in the

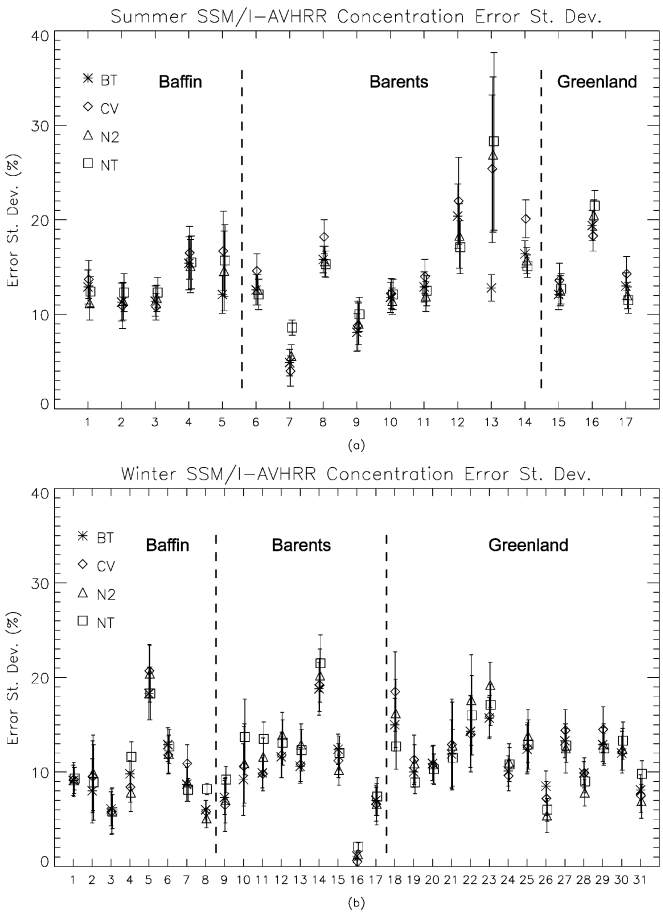


Fig. 3. Error standard deviation of SSM/I-derived concentrations relative to AVHRR concentrations (in percent) for (a) summer and (b) winter. The $x$ axis is the scene number as provided in Table I. Error bars represent the range of the 95% confidence level, as calculated using a bootstrap method.

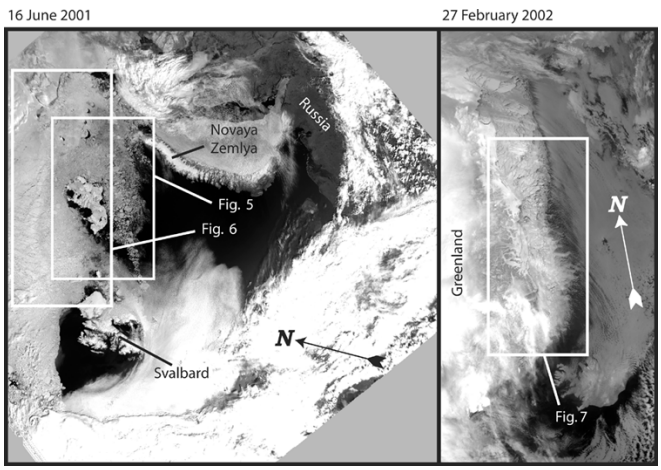


Fig. 4. Full AVHRR images for the case studies. (Left) AVHRR Channel 2 reflectance from the Barents Sea on June 16, 2001. Summer Scenes 6 and 7 (Figs. 5 and 6, respectively) are outlined in white. (Right) AVHRR Channel 4 radiance from the Greenland Sea on February 27, 2002, corresponding to Winter Scene 27 (Fig. 7). White corresponds to colder thermal temperatures.

Barents Sea scene on June 16, 2001, there is a clear dichotomy in ice conditions (Fig. 4). Thus, the analysis was split into two sections (i.e., scenes 6 and 7) (Figs. 5 and 6) to investigate the characteristics of the SSM/I concentrations in two ice regimes on the same day in roughly the same region.

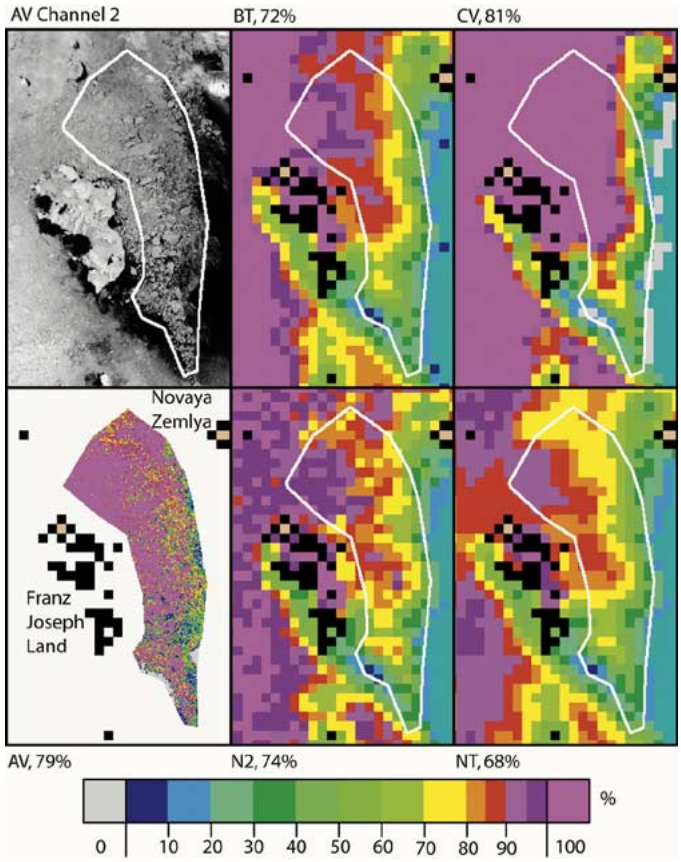


Fig. 5. Case study for the Barents Sea on June 16, 2001 (Summer Scene 6). Clockwise from top left are: 1) zoom of AVHRR channel 2 reflectance; 2) BT ice concentration; 3) CV ice concentration; 4) NT ice concentration; 5) N2 ice concentration; and 6) AVHRR ice concentration. The clear-sky region of the comparison, where AVHRR ice concentrations are computed, is outlined in white in the other fields. The color bar beneath the panels indicates ice concentrations at 10% intervals from 0% to 80% and 5% intervals from 80% to 100%; note that there is a separate color for 0% (gray) and 100% (light purple) concentrations. White corresponds to missing pixels, black to coastline, tan to land, and teal to open water (determined by the SSM/I weather filter). The numbers are the mean ice concentration for each algorithm.

In the more southern section (right side) of the Barents Sea image, in the area between Franz Joseph Land and Novaya Zemlya, the ice cover is broken with considerable open water between large and small floes (Fig. 5). The AVHRR concentration field clearly shows the individual large floes of 100% ice with scattered open water and small floes in between; AVHRR estimates total ice concentration of the area to be 79%. The SSM/I fields clearly cannot resolve the individual floes and the 25-km pixels represent an amalgam of floes. Typical of the statistical results, CV slightly overestimates the total concentration, while the other three algorithms underestimate it; NT has the largest negative bias with a value of $-11\%$. While CV has the smallest bias, it can be seen that the algorithm underestimates concentration near the bottom of the image, but near the top of the region, the concentration is a solid 100% and overestimates the areas of lower concentration indicated in AVHRR. This is due to the tendency of CV to saturate at high concentrations. In all four algorithms, the underestimation by SSM/I is primarily in the southernmost (right side) and western (bottom) part of the image, which is where the melting is likely most intense.

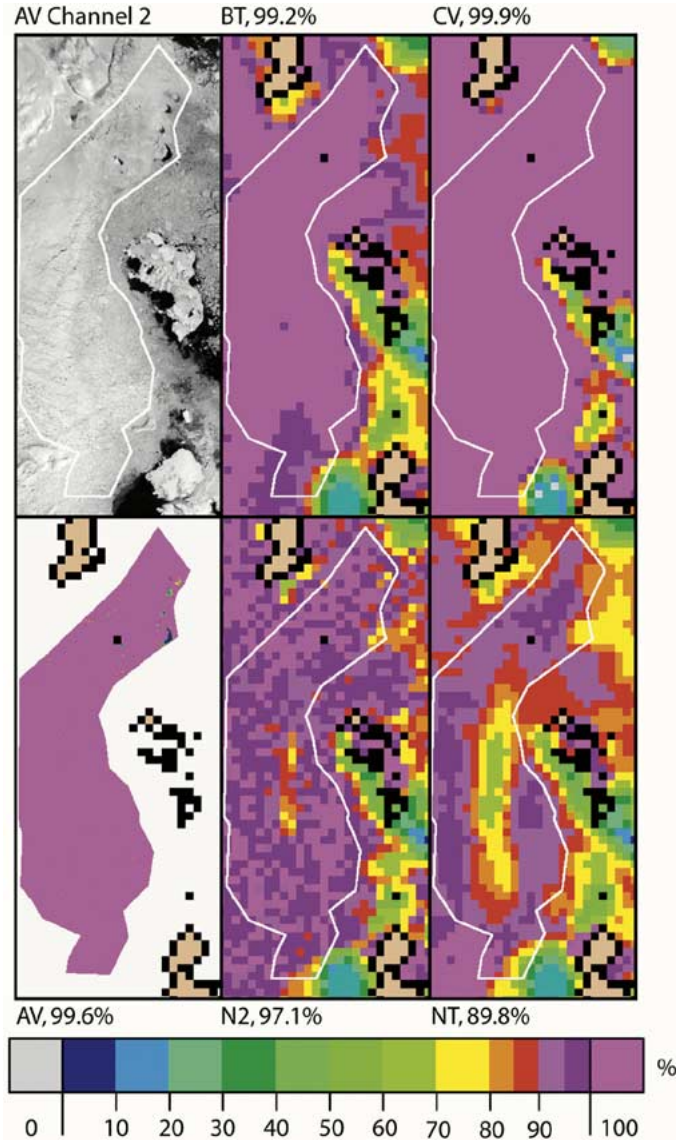


Fig. 6. Case study for the Barents Sea on June 16, 2001 (Summer Scene 7). Panels and colors are the same as in Fig. 5.

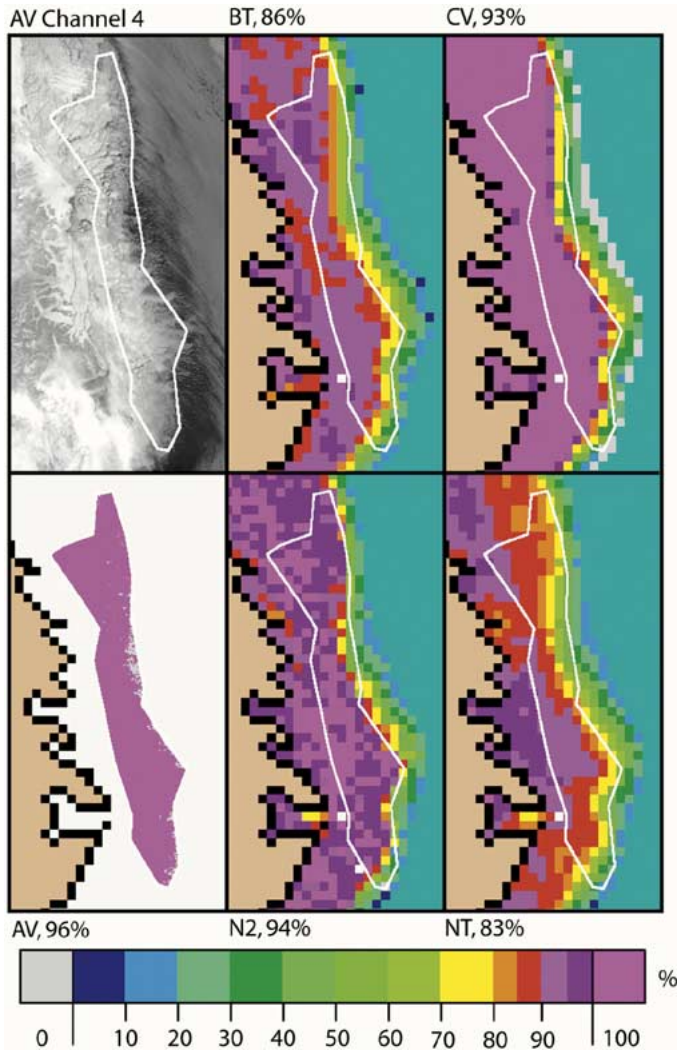


Fig. 7. Case study for the Greenland Sea on February 27, 2002 (Winter Scene 27). Panels and colors are the same as in Figs. 5 and 6.

While the southern part of the AVHRR scene (Fig. 5) has relatively loosely packed ice, the northern part of the scene (Fig. 6) encompasses a region of very compact ice. The higher albedo in this region compared to the area in Fig. 5 indicates that melt is not as intense. AVHRR indicates nearly 100% ice. Both BT and CV agree closely with the AVHRR estimate, with 100% ice except at the extreme bottom of the figure, near the ice edge. The underestimation by NT is quite startling, with a large area of depressed ice concentration in the center of the region where it is clear in the AVHRR image that the area is completely ice-covered.

Close inspection of the AVHRR image shows an apparent region of slightly higher albedo in the region of the underestimation by NT. A likely suspect for this would be a thin cirrus cloud. However, the low concentrations do not occur in either BT or CV. Since BT, CV, and NT all use the 19 V and 37 V GHz channels in their algorithms, while of the three only NT uses the 19 H GHz channel, it is likely that it is the 19 H channel causing the underestimation by NT. Since, this channel is less apt to be affected by the atmosphere than 37 V or 37 H [18], [20], it seems that the underestimation by NT is more likely a surface effect, perhaps a recent snowfall, or a melt-refreezing event. However, no ground truth is available to confirm this.

Regardless of the cause, this case study demonstrates the tendency for NT to underestimate ice conditions where BT and CV do not. The N2 algorithm is formulated similarly to NT and thus would be expected to have similar weaknesses. While there is indeed some reduced concentration in the same area as NT, the underestimation is much smaller. Thus, the addition of the 85-GHz channels ameliorates weaknesses in the NT algorithm and yields more realistic concentration estimates.

The better performance of N2 may be another indication that the feature causing errors in NT is a surface or near-surface feature. The 85-GHz channels are less sensitive to inhomogeneities, particularly within the snow overlying the ice, allowing the N2 fields to better handle the anomalous surface conditions [28]. In addition, the 85-GHz frequency is much more sensitive to atmospheric emission than the 19- and 37-GHz frequencies [18]. Thus, an atmospheric disturbance would be expected to show up more in the N2 fields than in

the NT fields although, as mentioned above, the N2 algorithm includes an atmospheric correction to remove such effects.

### B. Winter Case—Greenland Sea, February 27, 2002

The Greenland Sea is dominated primarily by thicker multiyear and first-year ice floes that have passed through Fram Strait. However, in winter, conditions are often conducive to new ice growth. This case study contains both of these elements (Fig. 7). Near the Greenland coast, the ice is mostly thick floes, but near the ice edge, there is thinner ice and new ice growth. There is also considerable cloud cover just off the ice edge. To avoid possible clouds, most of the eastern boundary of region was selected to be slightly inward of the ice edge. AVHRR indicates mostly 100% ice in the ice pack and some open water near the ice edge. All four SSM/I algorithms underestimate concentration, although both CV and N2 mean differences are quite small: 3% and 2%, respectively; BT and NT have negative biases of 10% or more. Thus, even in midwinter conditions, there is still the tendency to underestimate concentration near the ice edge.

In examining the fields in Fig. 7, much of the underestimation is close to the AHVRR ice edge. On the other hand, the SSM/I algorithms appear (qualitatively by visual inspection) to place the ice edge much farther east (to the right) than AVHRR, as much as four pixels (100 km). Both of these effects are at least partially due to the limitations of the large SSM/I footprint. As discussed above in Section VIII, the low resolution of SSM/I limits the ability to derive a precise ice edge, though we do not investigate ice edge errors in this study. Another factor could be the algorithms picking up emission by thin ice (or small thicker floes) east of the apparent AVHRR ice edge that does not appear in AVHRR due to clouds and the fact that the ice may have a temperature very close to freezing. In fact, surface air temperatures (not shown) from nearby Jan Mayen (slightly east of the ice edge), acquired from the National Climatic Data Center, indicate a recent influx of colder air, which would initiate new ice growth in the area.

## X. Effects of Clouds

A major limitation in evaluating SSM/I-derived concentration with concentration fields derived from visible and infrared imagery is that comparisons can only be made in clear sky conditions. Since the Arctic can be over 80% cloud-covered [40], [41], clouds are first a limiting factor in simply acquiring enough data points for representative comparisons. This study attempted to minimize this effect by collecting images from three regions encompassing nearly 10 million km$^2$ over nearly a year and by computing confidence levels.

A second limitation of clouds is that the clear-sky results are not indicative of performance under clouds. While clouds generally do not emit strongly in the 19- and 37-GHz channels, thicker clouds can potentially have a substantial effect on the observed brightness temperature and thus estimated concentration [19], [20]. Additionally, although the effect on the 19- and 37-GHz channels is generally small, this is not the case for the 85-GHz channels that the N2 uses. Thus, the good performance of the N2 found by this study may not be indicative of the performance under cloudy conditions. The N2 does perform an atmospheric correction that accounts for clouds and water vapor, but it is a fairly simple correction and may not work well in all conditions.

A quantitative evaluation of the performance of the SSM/I algorithms under cloudy conditions is not within the scope of this paper. However, inspection of the N2 fields compared to the other SSM/I fields in cloudy regions of the AVHRR imagery do not show any substantial degradation, although the high bias in sparse ice conditions (the $< 50\%$ regime in Table IX, likely near the ice edge where atmospheric influence is greater) is a possible indication of some degradation in N2 performance due to the atmosphere. To further investigate the potential effect of the atmosphere on N2, a related study was conducted where the SSM/I fields were compared to Radarsat imagery [42]. OLS visible/infrared imagery and observations from an ice breaker in the area [43] were used to select cloud-covered Radarsat scenes. While the case studies were qualitative in nature, the N2 fields did not appear to be significantly affected by the presence of clouds.

## XI. Summary and Conclusion

This study evaluating SSM/I-derived ice concentrations with AVHRR visible and infrared imagery recapitulates previous evaluations of Bootstrap and NASA Team algorithm estimates while encompassing two additional commonly used algorithms, the Cal/Val and NASA Team 2. This study focused on ice-covered regions near the ice edge where differences between the algorithms are expected to be largest. The results indicate that the NASA Team 2 has the smallest bias (relative to AVHRR), with the CV bias slightly larger. The NT, BT, and N2 tend to underestimate concentration, particularly during summer, while CV tends to overestimate concentration, also particularly during summer. The NT has the largest bias, with concentration estimates an average of nearly 10% too low. Most differences between the bias estimates of the algorithms are statistically significant at the 95% confidence level, based on a Monte Carlo bootstrap method.

The overall error standard deviations are 12% to 17%, with slightly larger values in the summer than in winter. The BT has the lowest error SD, but the results for the four algorithms are quite similar and few of the differences between the error SDs are significant at the 95% level. This indicates that the uncertainties in the concentration estimates (with respect to AVHRR concentrations) are largely algorithm-independent. Surface and atmospheric effects may affect all algorithms similarly and explain some of the similarity between the error SDs. However, because the algorithms use different combinations of frequencies, the major cause of the error SDs is likely to be the low spatial resolution of the SSM/I sensor not allowing the mixture of surface types within a pixel to be properly resolved.

While the statistical summaries are consistent, mean errors and error standard deviations vary substantially over the 17 summer and 31 winter scenes and on any given day, any of the four algorithms may yield the best results. Nonetheless, NT frequently has the largest bias and highest error SD and thus is the least reliable algorithm. Overall, CV and N2 have the lowest bias, although N2 has a high bias in regions with ice concentrations $< 50\%$, perhaps due to atmospheric effects.

Overall, BT has the lowest error SD and thus least uncertainty, although the difference between the BT and CV and N2 error SD values is not statistically significant.

Because much of the uncertainty in the passive microwave-derived sea ice concentrations is due to low spatial resolution, the advent of the AMSR-E sensor, with double the spatial resolution of SSM/I, should dramatically increase the accuracy of passive microwave ice concentration estimates. Additional frequencies on AMSR-E may also improve estimates. The N2 algorithm and a modified version of the BT algorithm have been selected as the primary algorithms for AMSR-E [44]. This study indicates that, overall, BT and N2 have lower biases and error standard deviations compared to the other algorithms, thus confirming that these are good selections for the AMSR-E products.

## ACKNOWLEDGMENT

The University Corporation for Atmospheric Research (funded by a NASA grant), the European Satellite Application Facility, and the Commander, U.S. Naval Meteorology and Oceanography Command provided support for this research. NOAA, the National Ice Center (NIC), and the Danish Meteorological Institute (DMI) supplied data and imagery. The National Snow and Ice Data Center provided information on the polar stereographic grid. Thanks to M. Chase (NIC) for SSM/I processing, S. Andersen (DMI) for AVHRR processing, and N. Bastar and M. Poukish (U.S. Naval Academy) for other data processing. Finally, thanks to the three anonymous reviewers and the editor for their helpful comments.

## REFERENCES

[1] J. C. Comiso, "A rapidly declining perennial sea ice cover in the Arctic," *Geophys. Res. Lett.*, vol. 29, no. 20, 1956.

[2] C. L. Parkinson, D. J. Cavalieri, P. Gloersen, H. J. Zwally, and J. C. Comiso, "Variability of Arctic sea ice, 1978–1996," *J. Geophys. Res.*, vol. 104, no. C9, pp. 20 837–20 856, 1999.

[3] O. M. Johannessen, E. V. Shalina, and M. W. Miles, "Satellite evidence for an Arctic sea ice cover in transformation," *Science*, vol. 286, pp. 1937–1939, 1999.

[4] P. Gloersen, C. L. Parkinson, D. J. Cavalieri, J. C. Comiso, and H. J. Zwally, "Spatial distribution of trends and seasonality in the hemispheric sea ice covers: 1979–1998," *J. Geophys. Res.*, vol. 104, no. C9, pp. 20 827–20 836, 1999.

[5] H. J. Zwally, J. C. Comiso, C. L. Parkinson, D. J. Cavalieri, and P. Gloersen, "Variability of Antarctic sea ice cover, 1978–1996," *J. Geophys. Res.*, vol. 107, no. C5, 2002.

[6] J. C. Comiso and K. Steffen, "Studies of Antarctic sea ice concentrations from satellite data and their applications," *J. Geophys. Res.*, vol. 106, no. C12, pp. 31 361–31 385, 2001.

[7] M. C. Serreze, J. A. Maslanik, T. A. Scambos, F. Fetterer, J. Stroeve, K. Knowles, C. Fowler, S. Drobot, R. G. Barry, and T. M. Haran, "A record minimum Arctic sea ice extent and area in 2002," *Geophys. Res. Lett.*, vol. 30, no. 3, 2003.

[8] J. A. Maslanik and M. C. Serreze, "On the record reduction in 1998 western Arctic sea-ice cover," *Geophys. Res. Lett.*, vol. 26, no. 13, pp. 1905–1908, 1999.

[9] K. C. Partington, "A data fusion algorithm for mapping sea-ice concentrations from special sensor microwave/imager data," *IEEE Trans. Geosci. Remote Sens.*, vol. 38, no. Jul., pp. 1947–1958, 2000.

[10] J. C. Comiso, D. J. Cavalieri, C. L. Parkinson, and P. Gloersen, "Passive microwave algorithms for sea ice concentration: A comparison of two techniques," *Remote Sens. Environ.*, vol. 60, pp. 357–384, 1997.

[11] G. Zibordi, M. Van Woert, G. P. Meloni, and I. Canossi, "Intercomparisons of sea ice concentration from SSM/I and AVHRR data of the Ross sea," *Remote Sens. Environ.*, vol. 53, pp. 145–152, 1995.

[12] W. J. Emery, C. Fowler, and J. A. Maslanik, "Arctic sea ice concentrations from special sensor microwave imager and advanced very high resolution radiometer satellite data," *J. Geophys. Res.*, vol. 99, no. C9, pp. 18 329–18 342, 1994.

[13] D. J. Cavalieri, "The validation of geophysical products using multisensor data," in *Microwave Remote Sensing of Sea Ice*, F. D. Carsey, Ed. Washington, DC: Amer. Geophys. Union, 1992, vol. 68, AGU Geophysical Monograph, pp. 233–242.

[14] K. Steffen and J. A. Maslanik, "Comparison of Nimbus 7 scanning multichannel radiometer radiance and derived sea ice concentrations with Landsat imagery for the north water area of Baffin Bay," *J. Geophys. Res.*, vol. 93, no. C9, pp. 10 769–10 781, 1988.

[15] R. Kwok, "Sea ice concentration estimates from satellite passive microwave radiometry and openings from SAR ice motion," *Geophys. Res. Lett.*, vol. 29, no. 9, 2002.

[16] T. Agnew and S. Howell, "The use of operational ice charts for evaluating passive microwave ice concentration data," *Atmos.-Ocean*, vol. 41, no. 4, pp. 317–331, 2003.

[17] K. Partington, T. Flynn, D. Lamb, C. Bertoia, and K. Dedrick, "Late twentieth century northern hemisphere sea-ice record from U.S. national ice center ice charts," *J. Geophys. Res.*, vol. 108, no. C11, 2003.

[18] D. T. Eppler *et al.*, "Passive microwave signatures of sea ice," in *Microwave Remote Sensing of Sea Ice*, F. D. Carsey *et al.*, Ed. Washington, DC: Amer. Geophys. Union, 1992, vol. 68, AGU Geophysical Monograph, pp. 47–71.

[19] C. Oelke, "Atmospheric signatures in sea-ice concentration estimates from passive microwaves: Modeled and observed," *Int. J. Remote Sens.*, vol. 18, no. 5, pp. 1113–1136, 1997.

[20] J. A. Maslanik, "Effects of weather on the retrieval of sea ice concentration and ice type from passive microwave data," *Int. J. Remote Sens.*, vol. 13, no. 1, pp. 37–54, 1992.

[21] J. Maslanik and J. Stroeve, *DMSP SSM/I Daily Polar Gridded Brightness Temperatures*. Boulder, CO: Nat. Snow and Ice Data Center, 2002.

[22] K. Steffen and A. Schweiger, "NASA team algorithm for sea ice concentration retrieval from the Defense Meteorological Satellite Program Special Sensor Microwave Imager: Comparison with Landsat imagery," *J. Geophys. Res.*, vol. 96, no. C12, pp. 21 971–21 987, 1991.

[23] J. Comiso, "Characteristics of Arctic winter sea-ice from satellite passive microwave and infrared observations," *J. Geophys. Res.*, vol. 91, no. C1, pp. 975–994, 1986.

[24] J. P. Hollinger, "DMSP Special Sensor Microwave/Imager calibration/validation," U.S. Nav. Res. Lab., Washington, DC, 1991.

[25] C. A. Bjerkelund, R. O. Ramseier, and I. G. Rubinstein, "Validation of the SSM/I and AES/York algorithms for sea ice parameters," in *Sea Ice Properties and Processes*, S. F. Ackley and W. F. Weeks, Eds. Hannover, NH: USACE, 1990, vol. 90-01, U.S. Army Cold Regions Research and Engineering Laboratory Monograph, pp. 206–208.

[26] D. J. Cavalieri, P. Gloersen, and W. J. Campbell, "Determination of sea ice parameters with the Nimbus 7 SMMR," *J. Geophys. Res.*, vol. 89, no. C3, pp. 5355–5369, 1984.

[27] D. J. Cavalieri, J. P. Crawford, M. R. Drinkwater, D. T. Eppler, L. D. Farmer, R. R. Jentz, and C. C. Wackerman, "Aircraft active and passive microwave validations of sea ice concentrations from the DMSP SSM/I," *J. Geophys. Res.*, vol. 96, no. C12, pp. 21 989–22 008, 1991.

[28] D. J. Cavalieri, "A microwave technique for mapping thin sea ice," *J. Geophys. Res.*, vol. 99, no. C6, pp. 12 561–12 572, 1994.

[29] T. Markus and D. J. Cavalieri, "An enhanced NASA team sea ice algorithm," *IEEE Trans. Geosci. Remote Sens.*, vol. 38, no. 3, pp. 1387–1398, May 2000.

[30] D. Lubin, C. Garrity, R. Ramseier, and R. H. Whritner, "Total sea ice concentration retrieval from the SSM/I 85.5 GHz channels during Arctic summer," *Remote Sens. Environ.*, vol. 62, pp. 63–76, 1997.

[31] L. Kaleschke, G. Heygster, C. Luepkes, A. Bochert, J. Hartmann, J. Haarpaintner, and T. Vihma, "SSM/I sea ice remote sensing for mesoscale ocean-atmosphere interaction analysis," *Can. J. Remote Sens.*, vol. 27, no. 5, pp. 526–537, 2001.

[32] S. Kern and G. Heygster, "Sea-ice concentration retrieval in the Antarctic based on the SSM/I 85.5 GHz polarization," *Ann. Glaciol.*, vol. 33, pp. 109–114, 2001.

[33] K. Tateyama, H. Enomoto, S. Takahashi, K. Shirasaki, K. Hyakutake, and F. Nishio, "New passive microwave remote sensing technique for sea ice in the sea of okhotsk using 85-GHz channel of DMSP SSM/I," *Bull. Glaciol. Res.*, vol. 17, pp. 23–30, 2000.

[34] P. Gloersen and D. J. Cavalieri, "Reduction of weather effects in the calculation of sea ice concentration from microwave radiances," *J. Geophys. Res.*, vol. 91, no. C3, pp. 3913–3919, 1986.

[35] D. J. Cavalieri, K. M. S. Germain, and C. T. Swift, "Reduction of weather effects in the calculation of sea ice concentration with the DMSP SSM/I," *J. Glaciol.*, vol. 41, no. 139, pp. 455–464, 1995.
[36] W. J. Emery, M. Radebaugh, C. W. Fowler, D. J. Cavalieri, and K. Steffen, "Comparison of sea ice parameters computed from advanced very high resolution radiometer and landsat satellite imagery and from airborne passive microwave imagery," *J. Geophys. Res.*, vol. 96, no. C12, pp. 22 075–22 085, 1991.
[37] K. Steffen and A. J. Schweiger, "A multisensor approach to sea ice classification for the validation of DMSP SSM/I passive microwave derived sea ice products," *Photogram. Eng. Remote Sens.*, vol. 56, pp. 75–82, 1990.
[38] W. N. Meier, M. L. Van Woert, and C. Bertoia, "Evaluation of operational SSM/I ice-concentration algorithms," *Ann. Glaciol.*, vol. 33, pp. 102–108, 2001.
[39] W. H. Press, S. A. Teukolsky, W. T. Vetterling, and B. P. Flannery, *Numerical Recipes in Fortran*, 2nd ed. Cambridge, U.K.: Cambridge Univ. Press, 1992, pp. 963–963.
[40] W. N. Meier, J. A. Maslanik, J. R. Key, and C. W. Fowler, "Multiparameter AVHRR-derived products for Arctic climate studies," *Earth Interactions*, vol. 1, no. 5, 1997.
[41] J. A. Curry, W. B. Rossow, D. Randall, and J. Schramm, "Overview of Arctic cloud and radiation characteristics," *J. Clim.*, vol. 9, no. 8, pp. 1731–1764, 1996.
[42] W. N. Meier, T. Maksym, and M. Van Woert, "Evaluation of operational microwave products: A case-study in the Barents Sea during October 2001," in *Ice in the Environment: Proc. Int. Assoc. Hydraulic Engineering and Research 16th IAHR Int. Symp. Ice*, vol. 3, Dunedin, New Zealand, Dec. 2–6, 2003, pp. 213–222.
[43] T. Maksym, private communication.
[44] J. C. Comiso, D. J. Cavalieri, and T. Markus, "Sea ice concentration, ice temperature, and snow depth using AMSR-E data," *IEEE Trans. Geosci. Remote Sens.*, vol. 42, no. 2, pp. 243–252, Feb. 2003.

**Walter N. Meier** received the B.S. degree in aerospace engineering from the University of Michigan, Ann Arbor, in 1991, and the M.S. and Ph.D. degrees in the interdisciplinary Program in Atmospheric and Oceanic Sciences (through the Aerospace Engineering Sciences Department) from the University of Colorado, Boulder, in 1992 and 1998, respectively.

Since then, he has been a Visiting Scientist at the U.S. National Ice Center, Suitland, MD, and an Adjunct Professor at the U.S. Naval Academy, Annapolis, MD. Since 2003, he has been a Research Scientist at the National Snow and Ice Data Center, Cooperative Institute for Research in the Environmental Sciences (CIRES), University of Colorado, Boulder, where his research focus is on the remote sensing of sea ice.